This version of the ESI published 13/07/2021 replaces the previous version published 07/10/2015. Figure S4(c) is replaced with a corrected version.

Electronic Supplementary Information

Ultrafast structural dynamics of in-cage isomerization of diiodomethane in solution

*Hanui Kim[a,b,c], Jong Goo Kim[c], Tae Wu Kim[c,g], Sang Jin Lee[a,b,c], Shunsuke Nozawa[d,e], Shin-ichi Adachi[d,e], Kihwan Yoon[f], Joonghan Kim[f], and Hyotcherl Ihee[a,b,c,]**

[a]Department of Chemistry, Korea Advanced Institute of Science and Technology (KAIST), Daejeon, 34141, Republic of Korea

[b]KI for the BioCentury, Korea Advanced Institute of Science and Technology (KAIST), Daejeon, 34141, Republic of Korea

[c]Center for Nanomaterials and Chemical Reactions, Institute for Basic Science (IBS), Daejeon, 34141, Republic of Korea

[d]Photon Factory, Institute of Materials Structure Science, High Energy Accelerator Research Organization (KEK), Tsukuba, Japan.

[e]Department of Materials Structure Science, School of High Energy Accelerator Science, The Graduate University for Advanced Studies, Tsukuba, Japan.

[f]Department of Chemistry, The Catholic University of Korea, Bucheon 14662, South Korea

[g](Present addresses) Chemical Sciences and Engineering Division, Argonne National Laboratory, Lemont, Illinois 60439, United States

Corresponding Author

*Hyotcherl Ihee: hyotcherl.ihee@kaist.ac.kr

TRXL data collection at SACLA

Time-resolved x-ray solution scattering measurements were performed at the BL3 beamline of SACLA. Femtosecond laser pulses at 800 nm center wavelength were generated from a Ti:sapphire regenerative amplifier and converted to 100 fs pulses at 267 nm wavelength by third-harmonic generation. The laser beam was focused by a lens to a spot of 0.8 mm diameter, where the laser beam was overlapped with the x-ray beam with the crossing angle of 10°. The x-ray pulses of sub-100 fs duration were generated at SACLA by self-amplified spontaneous emission (SASE). The x-ray pulses had center energy of 15 keV and an energy bandwidth narrow enough ($\Delta E/E = 0.6\%$) to monitor photoinduced structural changes of small molecules.[1, 2] The x-ray beam was focused on a spot of 0.2 mm diameter at the sample position. The scattering patterns generated by x-ray pulses were measured with an area detector (Rayonix LX255-HS) with a sample-to-detector distance of 29 mm. We used CH_2I_2 solution in methanol at a concentration of 50 mM. The sample solution was circulated through a sapphire nozzle with a 100 μm-thick aperture. To prevent the scattering signal from being contaminated by the radiation-damaged sample, the sample in the reservoir was replaced with a fresh sample whenever the reservoir sample failed to produce the known transient signal at 100 ps. Even if the transient signal at 100 ps did not change, the sample in the reservoir was replaced with a fresh one regularly (every 2–3 h of measurement) to ensure the delivery of fresh samples. The time resolution of the experiment, 540 fs, was limited by the timing jitter between the laser and x-ray pulses as well as a velocity mismatch of 120 fs, which was calculated by considering the laser/x-ray crossing angle of 10° and the sample thickness of 100 μm. The reference images were acquired with the x-ray pulse arriving 20 ps earlier than the laser pulse (that is, –20 ps time delay), to probe the (unexcited) molecules in the ground state while assuring the same average temperature of the sample solution. These reference images were repeatedly measured for every image at other time delays and were used as a reference

for calculating the time-resolved difference x-ray scattering patterns. To achieve a signal-to-noise ratio high enough for data analysis, about 150 images were acquired at each time delay. Each scattering image was obtained by accumulating scattering intensities of forty x-ray pulses. The data collection scheme of accumulating multiple x-ray shots in a single scattering image was enough to effectively suppress the fluctuation of signal caused by random pulse energies of the SASE process at SACLA. The scattering curves were measured at the following time delays: -10 ps, -9 ps, -8 ps, -7 ps, -6 ps, -5 ps, -4.5 ps, -4 ps, -3.5 ps, -3 ps, -2.5 ps, -2 ps, -1.5 ps, -1 ps, -0.5 ps, 0 ps, 0.5 ps, 1 ps, 1.5 ps, 2 ps, 2.5 ps, 3 ps, 3.5 ps, 4 ps, 4.5 ps, 6ps, 7 ps, 8 ps, 9 ps, 10 ps, 20 ps, 30 ps, 40 ps, 50 ps, 100 ps.

Generation of time-resolved difference scattering curves

Two-dimensional scattering images recorded on the CCD detector were azimuthally averaged to give one-dimensional scattering curves, $S(q, t)$, as a function of momentum transfer, q, and time delay, t, between the laser and x-ray pulses. Time-resolved difference scattering curves, $\Delta S(q, t)$, were generated by subtracting the reference data measured at –20 ps from the data at other time delays.

The two-dimensional scattering images can in principle have anisotropic components arising from the anisotropic orientational distribution of excited molecules. The difference scattering intensity of a two-dimensional difference scattering image can be decomposed as described in previous studies.[3] It can be seen in Figure S2 that the azimuthally-averaged difference scattering curves and the isotropic scattering curves, ΔS_0, are identical to each other within experimental errors. Thus, in this work, we used the azimuthally-averaged difference scattering curves, rather than isotropic difference scattering curves, without the need of accounting for the anisotropic contribution.

Comparison of the SACLA data and KEK data

To check the reproducibility of the x-ray scattering signals at SACLA, we compared time-resolved difference scattering curves, $q\Delta S(q, t)$, measured at SACLA and KEK as shown in Figure S3. The two difference scattering curves at 100 ps time delay measured at SACLA (red) and at 150 ps time delay measured at KEK (black) are nearly identical to each other within the experimental errors, indicating that the difference scattering curves are highly reproducible and independent of x-ray facilities.

Singular value decomposition (SVD) analysis and kinetic analysis

To determine the kinetic model of the photoexcitation reaction of CH_2I_2 and obtain the species-associated difference scattering curve (SADS) for each transient species, we applied an SVD analysis and a subsequent kinetic analysis to our experimental scattering data. From the time-resolved x-ray scattering data, we can build an $n_q \times n_t$ data matrix, **A**, where n_q is the number of q points in the scattering curves, and n_t is the number of time-delay points. The matrix **A** can be decomposed into three matrices while satisfying the relationship $\mathbf{A} = \mathbf{USV}^T$, where **U** is an $n_q \times n_t$ matrix whose columns are called left singular vectors (lSVs) (that is, time-independent q-spectra) of **A**, **V** is an $n_t \times n_t$ matrix whose columns are called right singular vectors (rSVs) (that is, amplitude changes with time of the lSVs in **U**) of A, and **S** is a diagonal $n_t \times n_t$ matrix whose diagonal elements are called singular values of **A** and can possess only non-negative values. The matrices **U** and **V** obey the relationships $\mathbf{U}^T\mathbf{U} = \mathbf{I}_{nt}$ and $\mathbf{V}^T\mathbf{V} = \mathbf{I}_{nt}$, respectively, where I_{nt} is the $n_t \times n_t$ identity matrix. The diagonal elements of S (that is, singular values) are ordered as $s_1 \geq s_2 \geq \ldots \geq s_n \geq 0$. Therefore, lSVs on the left side of **U** are supposed to have larger contributions to the experimental TRXL signal than those on the right side of **U**.

When linearly combined, the lSVs give information on the SADSs of transient states, whereas the rSVs contain the information on the population change of the transient states. Thus,

the SVD analysis provides a model-independent estimation of the number of structurally distinguishable transient states and contains information on the dynamics of each species. By performing the SVD analysis on our experimental difference scattering curves, $q\Delta S(q, t)$, we identified two singular components with significant singular values, indicating the existence of two transient states. The first two rSVs were globally fitted by one exponential function convoluted with a Gaussian function representing the instrument response function (IRF). As a result, we obtained an exponential with a time constant of 6.2 ± 0.8 ps and an IRF with a 540 ± 90 fs full-width at half-maximum (FWHM). Thus, we identified two transient states and one kinetic component connecting the two transient states.

To obtain SADSs of the two transient states identified in the SVD analysis, we performed a kinetic analysis on the **U** and **V** matrices using an appropriate kinetic model. First, using the result of the SVD analysis, we defined new matrices, **U′**, **V′** and **S′** that contain only the first two elements of **U**, **V**, and **S**. In other words, **U′** is an $n_q \times 2$ matrix containing only the first two lSVs of **U**, **S′** is a 2 × 2 diagonal matrix containing only the first two singular values of **S**, and **V′** is an $n_t \times 2$ matrix containing the first two rSVs of **V**. Among various kinetic models, the only one that can account for two transient states and one kinetic component is a sequential model. Therefore, by solving rate equations based on a sequential model, the concentrations of the two transient states can be calculated using the one kinetic component determined from the SVD analysis. We defined a matrix **C** that represents the time-dependent concentrations of the two transient states and related it to **V′** using a parameter matrix P that satisfies the relation $\mathbf{V'} = \mathbf{CP}$. In our analysis, **C** is an $n_t \times 2$ matrix containing the time-dependent concentrations of the two transient states, and **P** is a 2 × 2 matrix containing coefficients that relate the time-dependent concentrations of the transient states in **C** to the right singular vectors in **V′**. Once we determine **C** by solving the rate equations and convoluting

with the IRF, the theoretical solution scattering curves at various time delays, **A′**, can be generated as follows:

$$\mathbf{A'} = \mathbf{U'S'C'^{T}} = \mathbf{U'S'(CP)^{T}} = \mathbf{U'S'(P^{T}C^{T})} = \mathbf{(U'S'P^{T})C^{T}} \quad \text{(S1)}$$

The matrix **P** can be optimized by minimizing the discrepancy, χ^2, between the theoretical and experimental difference scattering curves:

$$\chi^2 = \sum_{i=1}^{n_q}\sum_{j=1}^{n_t}\left(\frac{q\Delta S_{\exp}(q_i,t_j) - q\Delta S_{theory}(q_i,t_j)}{q\sigma_{ij}}\right)^2 \quad \text{(S2)}$$

where $\Delta S_{\exp}(q_i, t_j)$ and $\Delta S_{\text{theory}}(q_i, t_j)$ are the experimental and theoretical difference scattering curves at given q and t values, respectively, and σ_{ij} is the experimental standard deviation at given q and t values. From equation (1), we can define a matrix **B** as $\mathbf{B} = \mathbf{U'S'P^{T}}$. As a result, **B**, an $n_q \times 2$ matrix, contains the difference scattering curves directly associated with the transient states. Thus, by optimizing **P**, we obtain the time-independent, SADSs of the transient states (optimized **B**).

As a result, we obtained two SADSs shown in Figure S5a and a single time constant of 6.2 ± 0.8 ps for the conversion from the first species to the second species as shown in Figure S5b. It turned out the SADS1 and the SADS2 are the same as the difference scattering patterns measured at 0.5 ps and 100 ps, respectively, within our experimental error as shown in Figure S6.

As shown in Figure S5b, SADS2 is identical to the difference scattering curve at 150 ps time delay measured at KEK within the experimental error. According to the TRXL study at KEK,[4] there exist the two intermediate species at 150 ps, $CH_2I\bullet$ + I• radical (46 %) and CH_2I-I isomer (54 %), suggesting that the signal of SADS2 also arises from two intermediate species. Here $CH_2I\bullet$ + I• denotes the $CH_2I\bullet$ and I• photofragments that are completely separated and not in the same solvent cage. When SADS2 is fitted with the fraction and I-I distance of CH_2I–I

isomer as fitting parameters, the best fit yielded 53.9 ± 5.2 % and 3.15 ± 0.02 Å, which are consistent with the previous result (54 % and 3.15 Å), and the theoretical difference scattering curve generated with these known parameters gives an excellent agreement with experimental SADS2 as shown in Figure 2c. This result means that the CH_2I–I isomer and CH_2I• + I• are formed with a time constant of 6.2 ps via the conversion from the species generated at the onset of the reaction. Accordingly, the time constant must be responsible for the formation of either the CH_2I-I isomer or CH_2I• + I•. Among these two possibilities, it is highly likely that the isomer is formed with the observed time constant of 6.2 ps because 6.2 ps agrees well with the values (5 ps in TA,[5-7] 4-50 ps time scales in TRR[8-11]) reported for the isomer formation in the previous spectroscopic studies. In this scenario, both CH_2I• + I• and the precursor of the isomer must have formed initially upon excitation and the precursor of the isomer converts to the isomer with the time constant of 6.2 ps. This scenario also implies that the branching ratio of 54:46 observed at 100 ps is already determined at the onset of the reaction.

Structural fitting analysis

The difference scattering curves of CH_2I_2 in methanol shown in Figure 2 can be explained by the sum of three components: (i) solute-only term, (ii) cage term, and (iii) solvent-only term as follows:

$$\Delta S(q,t) = \Delta S_{solute}(q,t) + \Delta S_{solute-solvent}(q,t) + \Delta S_{solvent}(q,t) \quad \text{(S3)}$$

The solute-only term was calculated with the Debye equation based on the structures of solute molecules.

$$S(q) = \sum_n f_n^2(q) + \sum_n \sum_{m \neq n} f_n(q) f_m(q) \frac{\sin qr_{nm}}{qr_{nm}} \quad \text{(S4)}$$

where $f_n(q)$ and $f_m(q)$ are the atomic form factors of the n-th and m-th atom and r_{nm} is the distance between the n-th and m-th atoms.

Since it is known that the pathways of photodissociation of CH_2I_2 branches into CH_2I-I isomer and $CH_2I\bullet$ + I• radical, an additional parameter is introduced as follows:

$$\Delta S_{solute}(q) = \mathrm{f}S_{isomer}(q) + (1\text{-}\mathrm{f})S_{radical}(q) - S_{ground}(q) \quad \text{(S5)}$$

where f:(1-f) is the branching ratio between the isomer and radical, which was determined as 54:46 in our previous study.[4] The structure of ground-state CH_2I_2, $CH_2I\bullet$ radical, and CH_2I-I isomer and the value for the branching ratio (54:46) were adapted from our previous study.[4] During the structural fitting analysis, the structure of the loosely-bound radical pair was determined by optimizing the I-I distance and the C-I-I angle as free fitting parameters.

The cage term, solute-solvent cross term, was calculated from the pair distribution functions ($g(r)$) obtained from molecular dynamics (MD) simulations. Partial atomic charges were obtained from DFT calculation and used for the simulation. For the loosely-bound isomer precursor, partial charge obtained from CH_2I-I isomer was used. The cage term for the loosely bound isomer precursor was obtained by an iterative calculation. Firstly, we generated the cage term without applying any DWF to the loosely bound isomer precursor. Then we used this cage term to fit the DWF and structure of the precursor. Using the refined structure of the precursor, a new cage term was then calculated and used in the subsequent refinement. We repeated this procedure until the σ^2 of DWF value converged.

The solvent-only term was obtained by a separate solvent heating experiment using a ferrocene solution with the same experimental conditions. The measured scattering signal arose from the heating of a pure solvent induced by laser excitation. In the structural fitting analysis, the contribution from the heating was calculated by the experimental heating curve times a free fitting parameter. The values of this parameter from the best fit represent the amount of the heating at each delay point. The amount of the heating at each time delay is converted to the temperature change of solvent[4] and the time-dependent temperature changes are shown in Figure S7.

The structural fitting results for SADS1 are shown in Figure 2b. In this case, the I–I distance ($R_{I\text{-}I}$) and the C-I-I angle were used as structural fitting parameters. The fit with the lowest discrepancy with the experimental SADS1 (Figure 2b, red dashed line) gives $R_{I\text{-}I}$ of 6.27 Å, which is about 2.69 Å longer than that of the ground state. However, even though this fit result is the best available one obtained from our analysis protocol, the quality of the fit is much worse than that of SADS2 and not enough to be considered as a satisfactory answer, indicating that the structural analysis scheme for SADS1 needs to be improved to accurately describe the structure of the precursor of the isomer.

This consideration suggests that our analysis protocol used here with the assumption that the I–I pair has a well-defined distance may not work well in this case. Therefore, to describe the relatively free movement of the weakly bound I atom, we incorporated a Debye-Waller factor (DWF),[12, 13] $\exp(-\sigma^2 q^2/2)$, involving the mean-squared displacement (σ^2) for $R_{I\text{-}I}$ into the equation for calculating the theoretical scattering pattern (see the following section for details). Normally, since the broadening of an atomic pair on the TRXL signal imposed by the form factor itself is much larger than the broadening caused by thermal vibration, the latter has a negligible effect for a regular chemical bond. For this reason, a DWF generally does not need to be considered in the typical structure analysis of TRXL data, which means that $\sigma^2 = 0$ and DWF = 1.

Structural fitting analysis with a Debye-Waller factor

In order to consider the effect on the scattering signal imposed by the broad distribution of I-I distance, we incorporated a Debye-Waller factor (DWF), $\exp(-\sigma^2 q^2/2)$, for the I-I distance by modifying the equation for calculating the theoretical scattering pattern as follows:

$$S(q) = \sum_n f_n^2(q) + \sum_n \sum_{m \neq n} f_n(q) f_m(q) \frac{\sin qr_{nm}}{qr_{nm}} \exp(-\sigma^2 q^2 / 2) \qquad \text{(S6)}$$

where σ^2 is the mean-squared displacement and used as an additional free fitting parameter. According to the equation S6, the use of DWF mainly affects the scattering signal in the wide angle region. However, since $R_{I\text{-}I}$ also depends on the σ^2 value of DWF for the I-I distance during the structural fitting analysis to find the optimal fit, the fitting quality improves for the overall *q*-range as shown in Figure 2b.

The use of DWF for the I-I distance assumes that the distribution of the distance is nearly symmetric. In order to simulate the possible asymmetric distribution of the I-I distance, we also fit with multiple I-I distances and the results are shown in Figure S9. Even when two I-I distances were considered as free fitting parameters, the two I-I distances became similar and the quality of the fit did not improve. The broad distribution in the C-I distance is also expected for the isomer precursor However, due to the relatively lower sensitivity compared to the I-I distance, the use of DWF for C-I distance did not improve the quality of the fit as shown in Figure S10.

Structural fitting analysis with a dynamic model

We tested if our experimental data can be also well explained by a dynamic model instead of the simple kinetic model. We set a model showing a gradual change of the structural parameters including the DWF and I-I distance of the isomer precursor with the 6.2 ps time constant. The quality of the fit is compared with the one with the simple kinetic model in Figure S11. A dynamic model failed to explain our experimental data and the best fit is achieved when the simple kinetic model is used. It should be noted, however, that this result does not necessarily mean that such a dynamic process where the DWF and I-I distance change with time is not correct. With an improved time resolution compared with that used in this study (~540 fs), a more dynamic picture may emerge from the TRXL data.

Computational Details

Geometry optimizations of the triplet states of radical pairs ($CH_2I\bullet\cdots I\bullet$) and the parent molecule of CH_2I_2 were performed using coupled-cluster singles and doubles with perturbative triples (CCSD(T)). The minimum energy structures were identified via harmonic vibrational frequency calculations. The calculations with the frozen-core approximation lead to occurring of an imaginary frequency of the triplet state of the radical pair. Thus, all electrons were correlated in the CCSD(T) calculations. The scalar relativistic effects for I atoms were treated using the relativistic effective core potential (RECP). The valence electrons of I were calculated using the aug-cc-pVTZ basis set. The all-electron basis sets (aug-cc-pVTZ) were used for other atoms, C and H. Hereafter, this combination is denoted as AVTZ. The solvent (methanol) effect was considered using the integral equation formalism polarizable continuum model (IEFPCM). The single-point calculations were also performed with quadruple zeta basis sets (AVQZ) to obtain accurate energetics. The T_1 diagnostic values of all CCSD(T) calculations were less than 0.02, indicating that multireference character is insignificant. Therefore, CCSD(T) is an adequate method for calculating the triplet states of radical pairs. All calculations were performed using the Gaussian16 program.

Discussion on the computed structures of radical pairs

While the concept of the radical pair has been frequently discussed in the literature, the exact structural aspect has never been determined. Since we obtained experimental evidence for the structure of the radical pair, we performed CCSD(T) calculations to provide computational support for the radical pair as well as to compare the experimental and computational results. The difficulty to characterize $CH_2I\bullet\cdots I\bullet$ in the solvent cage originates from the weak interaction in the radical pair. The theoretical characterization of the weakly bound molecule is not trivial because of the difficulty in describing the weak interaction via

the quantum chemical methods. In addition, the singlet state molecule with a long bond length has significant non-dynamic electron correlation effects. Therefore, the multireference based quantum chemical methods are necessary for the calculation of the singlet state of the radical pair. However, such methods do not have an analytical gradient technique and cannot incorporate the solvent effect. These difficulties may explain the lack of theoretical studies for the radical pair. Our attempts of geometry optimizations of the singlet states of $CH_2I\bullet\cdots I\bullet$ have also failed; the calculated results converged to the parent molecule (CH_2I_2) or the CH_2I-I isomer. Therefore, we switched to the triplet states of $CH_2I\bullet\cdots I\bullet$ in performing the CCSD(T)/AVTZ calculations and succeeded in finding the two molecular structures named RP1 ($^3A_2$ state) and RP2 ($^3A'$ state) of the triplet state of $CH_2I\bullet\cdots I\bullet$ (Figure S12). According to our calculations (CCSD(T)/AVQZ//CCSD(T)/AVTZ), the binding energies including the zero-point energy (enthalpy in bold) of RP1 and RP2 with respect to $CH_2I\bullet$ + $I\bullet$ are 2.3 (**2.4**) and 6.4 (**6.6**), respectively, indicating the nature of the loosely-bound structures. In addition, as shown in Figure S12, the $R_{I\text{-}I}$ of RP1 and RP2 are 3.928 Å and 3.349 Å, respectively. Especially the $R_{I\text{-}I}$ of RP1 is close to that (4.17 Å) determined by TRXL in this work. We found the $^3A''$ state whose $R_{I\text{-}I}$ is 4.559 Å (Figure S12), but it is a transition state that has a small magnitude of an imaginary frequency (46*i* cm^{-1}). With more sophisticated methods, this structure may turn out to be a local minimum and there might be many such loosely-bound local minima. In this regard, the real molecular structure of the triplet states of the radical pair would be the thermally averaged one of the various local minima. Such an averaged structure would be consistent with the unusually large σ^2 (0.45 $Å^2$) obtained from the TRXL data.

We calculated the Mulliken spin densities to identify the locations of unpaired electrons of RP1 and RP2 and they are shown in Figure S12. As shown in Figure S12, the up spin densities of RP1 and RP2 are located in the I• and C of $CH_2I\bullet$, which supports that indeed they are the radical pairs. Moreover, the singlet state calculations starting from RP1 and RP2

converged to the parent molecule or the isomer for the optimal structures. These results indicate that the origin of the triplet states of radical pairs is the Pauli repulsion between the up spins. The energy decomposition analysis (EDA) is necessary for the details, but EDA for the correlated ab initio methods is not available yet.

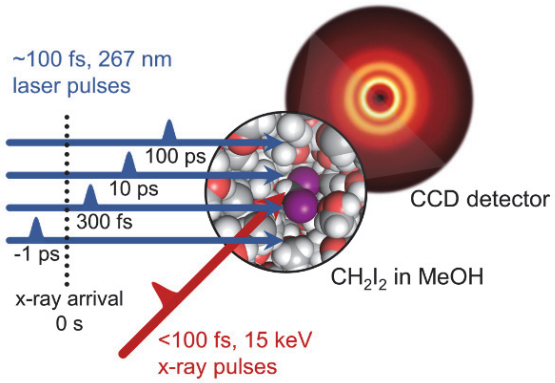

Figure S1. Schematic diagram of femtosecond TRXL measurement of CH_2I_2 in methanol. The photochemical reaction of solutes is triggered by a femtosecond optical laser pulse. Subsequently, a time-delayed x-ray pulse synchronized with the laser pulse probes the structural dynamics of the reaction. The scattering pattern is detected by a fast two-dimensional CCD detector. We measure time-resolved scattering patterns at various time delays between the laser and x-ray pulses.

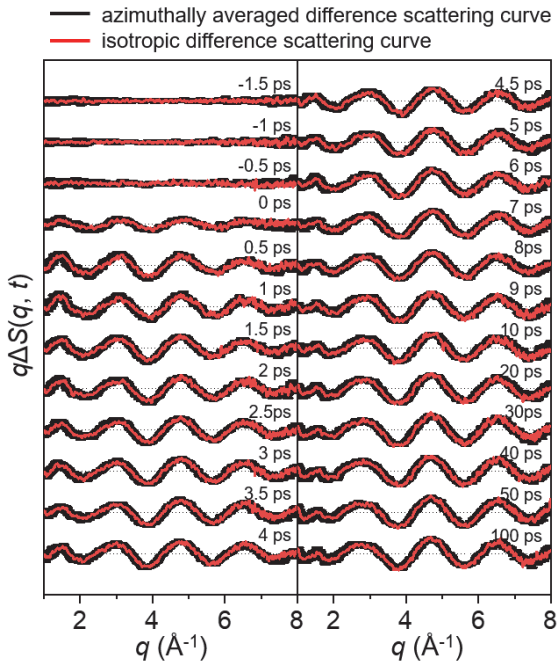

Figure S2. Time-resolved difference scattering curves, $q\Delta S(q, t)$, of CH_2I_2 in methanol obtained by the azimuthal average of two-dimensional scattering images (black). For comparison, isotropic difference scattering curves were generated from the scattering images (red). The two data sets are identical to each other within experimental errors, indicating that azimuthally averaged difference curves used in this work are practically identical to the isotropic difference scattering curves. For further data analysis, the azimuthally averaged difference curves were used since they have actually measured experimental errors and a better signal-to-noise ratio.

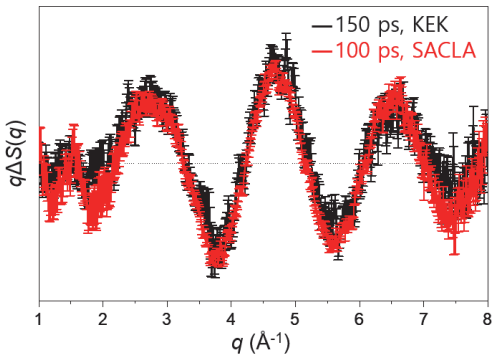

Figure S3. Comparison of the difference scattering curves at 150 ps time delay measured at KEK (black) and at 100 ps time delay measured at SACLA (red). The two curves are nearly identical to each other within the experimental errors, indicating that the difference scattering curves are highly reproducible and independent of x-ray facilities.

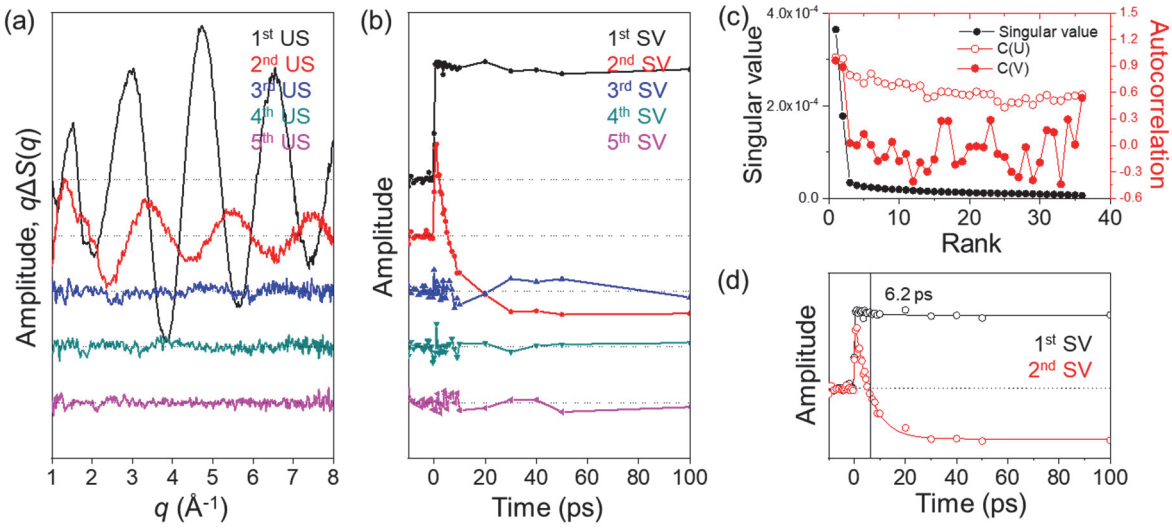

Figure S4. Results of SVD analysis. (a) The first five lSVs multiplied by singular values. (b) The first five rSVs multiplied by singular values (c) Singular values (S, black solid circle), autocorrelations of lSVs (C(U), red open circle) and autocorrelations of rSVs (C(V), red solid circle) (d) The first two rSVs multiplied by singular values were globally fitted by a single exponential function convoluted with a Gaussian function representing the IRF, yielding the time constant of 6.2 ± 0.8 ps and an IRF with a 540 ± 90 fs FWHM.

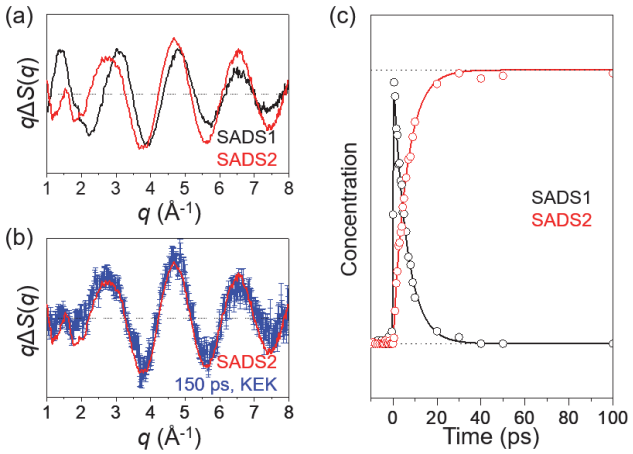

Figure S5. Results of kinetic analysis. (a) SADSs of two states. (b) Comparison of SADS2 (red) and the difference scattering curve of 150 ps measures at KEK (blue). The two curves are identical within the experimental error. According to the TRXL result at KEK, there exist the two intermediate species at 150 ps, $CH_2I\bullet$ + I• (46 %) and CH_2I-I isomer (54 %), meaning that the signal of SADS2 arises from these two intermediate species. (c) Time-dependent concentrations of the two states. The lines correspond to the concentrations obtained from the kinetic analysis. Dots correspond to the coefficients of SADSs obtained by fitting the experimental curve at each time point with a linear combination of SADSs.

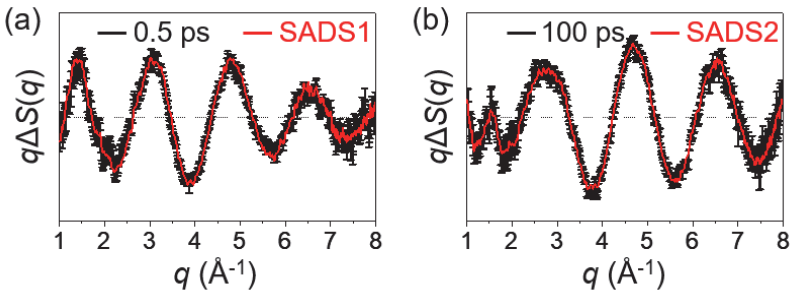

Figure S6. (a) Comparison of the difference scattering curve of 0.5 ps time delay (black) and SADS1 (red). (b) Comparison of the difference scattering curve of 100 ps time delay (black) and SADS2 (red). SADS1 and SADS2 are the same as the difference scattering patterns measured at 0.5 ps and 100 ps, respectively, within the experimental errors.

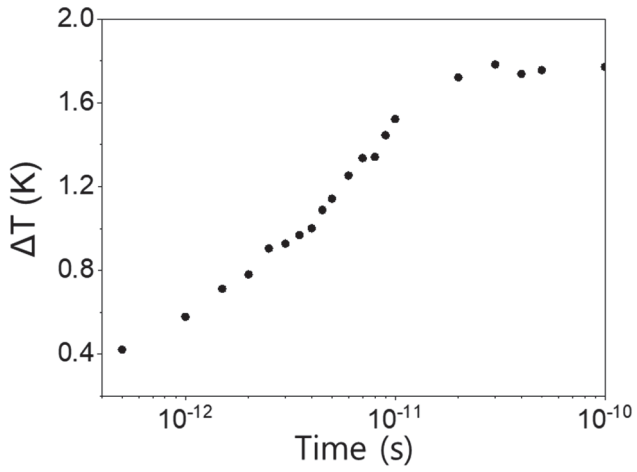

Figure S7. Time-dependent changes of solvent temperature.

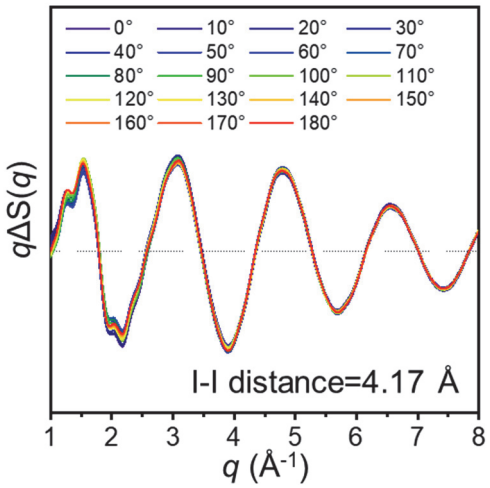

Figure S8. Theoretical difference scattering curves obtained for various C-I-I angle of the loosely-bound isomer precursor from 0° to 180° with the I-I distance fixed at 4.17 Å. The difference scattering curves do not show a strong dependence on the C-I-I angle, indicating that they are not so sensitive to the C-I-I angle of the loosely-bound isomer precursor.

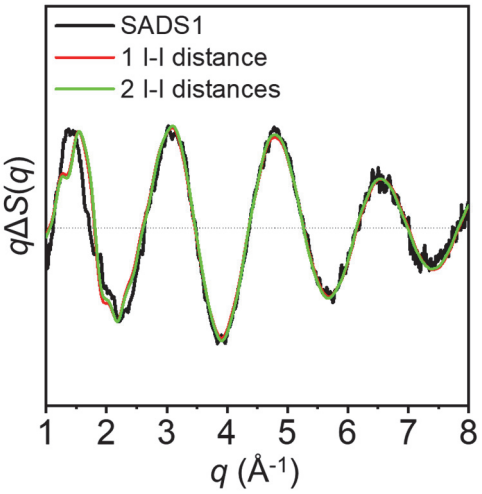

Figure S9. One (red) and two (green) I-I distances were used for the structural fitting analysis to simulate the possible asymmetric distribution of the I-I distance of the precursor of isomer. Even when two I-I distances were considered as free fitting parameters, the two I-I distances became similar and the quality of the fit did not improve.

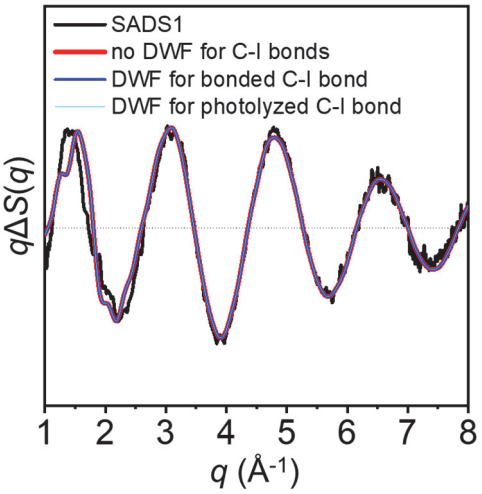

Figure S10. The structural fitting analysis with (blue and cyan) and without (red) the use of DWF for C-I distances. The use of DWF for C-I bonds did not improve the quality of the fit.

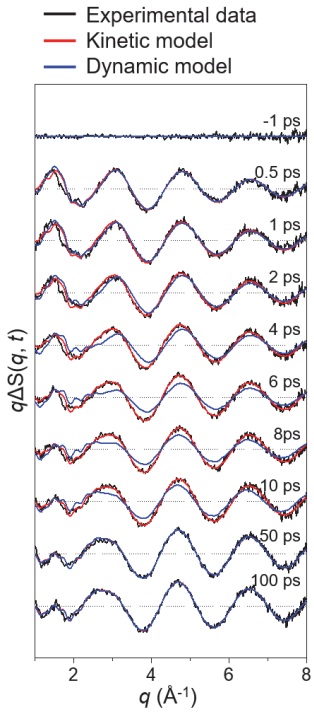

Figure S11. Assessment of the quality of the fit depending on the model employed for the fit. The best fit is achieved when the simple kinetic model is used.

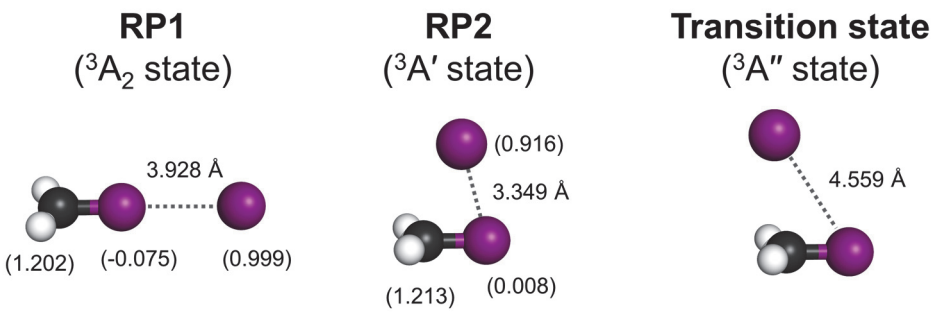

Figure S12. Structures and Mulliken spin densities (given in parentheses) of the radical pairs in the triplet state optimized by CCSD(T)/AVTZ calculations. The optimized $^3A_2$ and $^3A'$ states of the radical pair are named as RP1 and RP2, respectively. The $^3A''$ state is optimized as a transition state that has a small magnitude of an imaginary frequency (46i cm^{-1}).

Table S1. Relative χ^2 value ($\chi^2_{relative}$) obtained from the structural fitting analysis. The relative χ^2 value is the χ^2 value divided by that of the best fit for SADS1 or SADS2.

	SADS1		SADS2	
	Without DWF	With DWF	Without DWF	With DWF
$\chi^2_{relative}$	6.61	1	1.01	1

Table S2. Optimized structural parameters of the chemical species involved in the CH_2I_2 photodissociation.

	Ground (CH_2I_2)	Loosely-bound isomer precursor ($CH_2I\cdots I$)	Isomer (CH_2I-I)	Radical ($CH_2I\bullet$)
C-I distance [a] (Å)	2.13 [b]	1.98 [b]	1.98 [b]	2.04 [b]
I-I distance (Å)	3.58 [b]	4.17 (± 0.23)	3.15 [b]	-
σ^2 of DWF in $R_{I\text{-}I}$ ($Å^2$)	0 [b]	0.45 (± 0.22)	1.2×10^{-3} ($\pm 0.2\times10^{-3}$)	-
C-I-I angle (°)	32.6 [b]	79.4 (± 1.6)	115.0 [b]	-

[a] C-I distance represents the bond distance between C and the unphotolyzed I atom.

[b] Parameters are adapted from the previous study.[4]

Reference

1. Y. Inubushi, K. Tono, T. Togashi, T. Sato, T. Hatsui, T. Kameshima, K. Togawa, T. Hara, T. Tanaka, H. Tanaka, T. Ishikawa and M. Yabashi, *Phys. Rev. Lett.*, 2012, **109**, 144801.

2. T. Ishikawa, H. Aoyagi, T. Asaka, Y. Asano, N. Azumi, T. Bizen, H. Ego, K. Fukami, T. Fukui, Y. Furukawa, S. Goto, H. Hanaki, T. Hara, T. Hasegawa, T. Hatsui, A. Higashiya, T. Hirono, N. Hosoda, M. Ishii, T. Inagaki, Y. Inubushi, T. Itoga, Y. Joti, M. Kago, T. Kameshima, H. Kimura, Y. Kirihara, A. Kiyomichi, T. Kobayashi, C. Kondo, T. Kudo, H. Maesaka, X. M. Maréchal, T. Masuda, S. Matsubara, T. Matsumoto, T. Matsushita, S. Matsui, M. Nagasono, N. Nariyama, H. Ohashi, T. Ohata, T. Ohshima, S. Ono, Y. Otake, C. Saji, T. Sakurai, T. Sato, K. Sawada, T. Seike, K. Shirasawa, T. Sugimoto, S. Suzuki, S. Takahashi, H. Takebe, K. Takeshita, K. Tamasaku, H. Tanaka, R. Tanaka, T. Tanaka, T. Togashi, K. Togawa, A. Tokuhisa, H. Tomizawa, K. Tono, S. Wu, M. Yabashi, M. Yamaga, A. Yamashita, K. Yanagida, C. Zhang, T. Shintake, H. Kitamura and N. Kumagai, *Nat. Photon.*, 2012, **6**, 540-544.

3. J. G. Kim, S. Nozawa, H. Kim, E. H. Choi, T. Sato, T. W. Kim, K. H. Kim, H. Ki, J. Kim, M. Choi, Y. Lee, J. Heo, K. Y. Oang, K. Ichiyanagi, R. Fukaya, J. H. Lee, J. Park, I. Eom, S. H. Chun, S. Kim, M. Kim, T. Katayama, T. Togashi, S. Owada, M. Yabashi, S. J. Lee, S. Lee, C. W. Ahn, D.-S. Ahn, J. Moon, S. Choi, J. Kim, T. Joo, J. Kim, S.-i. Adachi and H. Ihee, *Nature*, 2020, **582**, 520-524.

4. S. Park, J. Choi, H. Ki, K. H. Kim, K. Y. Oang, H. Roh, J. Kim, S. Nozawa, T. Sato, S. I. Adachi, J. Kim and H. Ihee, *J. Chem. Phys.*, 2019, **150**, 224201.

5. A. N. Tarnovsky, J. L. Alvarez, A. P. Yartsev, V. Sundstrom and E. Akesson, *Chem. Phys. Lett.*, 1999, **312**, 121-130.

6. A. N. Tarnovsky, V. Sundstrom, E. Akesson and T. Pascher, *J. Phys. Chem. A*, 2004, **108**, 237-249.

7. K. Saitow, Y. Naitoh, K. Tominaga and K. Yoshihara, *Chem. - Asian J.*, 2008, **3**, 696-

709.

8. W. M. Kwok, C. S. Ma, A. W. Parker, D. Phillips, M. Towrie, P. Matousek and D. L. Phillips, *J. Chem. Phys.*, 2000, **113**, 7471-7478.

9. X. M. Zheng and D. L. Phillips, *J. Phys. Chem. A*, 2000, **104**, 6880-6886.

10. Y. L. Li, D. Q. Wang, K. H. Leung and D. L. Phillips, *J. Phys. Chem. A*, 2002, **106**, 3463-3468.

11. X. Guan, X. Lin, W. M. Kwok, Y. Du, Y. L. Li, C. Zhao, D. Wang and D. L. Phillips, *J. Phys. Chem. A*, 2005, **109**, 1247-1256.

12. I. Hargittai and M. Hargittai, *Stereochemical applications of gas-phase electron diffraction / Part A: the electron diffraction Technique.*, VCH, Weinheim, 1988.

13. H. Yong, J. M. Ruddock, B. Stankus, L. Ma, W. Du, N. Goff, Y. Chang, N. Zotev, D. Bellshaw, S. Boutet, S. Carbajo, J. E. Koglin, M. Liang, J. S. Robinson, A. Kirrander, M. P. Minitti and P. M. Weber, *J. Chem. Phys.*, 2019, **151**, 084301.